Article

Ocean Color Image Sequences Reveal Diurnal Changes in Water Column Stability Driven by Air–Sea Interactions

Jason K. Jolliff * , **Travis A. Smith, Sherwin Ladner, Ewa Jarosz, Mark David Lewis, Stephanie Anderson, Sean McCarthy and Adam Lawson**

Naval Research Laboratory, Stennis Space Center, MS 39529, USA
* Correspondence: jason.jolliff@nrlssc.navy.mil

Abstract: The southward propagation of cold-air frontal boundaries into the Gulf of Mexico region initiates a cascade of coupled air–sea processes that manifests along the coastlines as an apparent brightness anomaly in the ocean color signals. Our hypothesis is that the color anomaly is largely due to the turbulent resuspension of sedimentary particles. Initially, there is significant wind-driven ocean turbulence as the frontal boundary passes, followed by the potential for sustained convective instability due to significant heat losses from the ocean surface. These cold front events occur during boreal autumn, winter, and into early spring, and the latter episodes occur in the context of the seasonally recurring thermal stratification of shelf waters. Here, we show that as stratification reasserts thermal stability in the waning days of a cold front episode, daily to hourly ocean color patterns are temporally coherent with the air–sea heat flux changes and the resulting impact on water column stability. Concomitant results from a nested, data-assimilative, and two-way coupled ocean-atmosphere numerical modeling system provides both corroboration and insight into how surface air–sea fluxes and in-water turbulent mixing manifest as hourly changes in apparent surface water turbidity due to the potential excitation and settling of reflective particles. A simple model of particle mixing and settling driven by the simulated turbulence mimics patterns seen in the satellite image sequences. This study offers a preview of potential application areas that may emerge following the launch of a dedicated ocean color geostationary sensor.

Keywords: ocean color; coastal oceanography; air–sea interactions; turbidity; satellite oceanography

1. Introduction

The cold air masses originating over the North American continent penetrate south across the Gulf of Mexico with increasing frequency from approximately November through to April [1–5]. These high-frequency meteorological events (~50 or more episodes each year) are characterized by an initial increase in wind velocity towards the south followed by a sustained drop in air temperatures (>10 °C) [6]. Referred to as cold-air outbreak (CAO) events [1,7], or nortes [8], these episodes have a significant impact upon the oceanography of the region—the principal effect being the destruction of thermal stratification [9]. Thus, CAO events play an important role in the seasonal oceanographic transition from warm, stratified to cool and well-mixed surface waters, particularly in shallower areas over the continental shelves (<100 m depth).

In a previous paper, it was demonstrated that over the West Florida continental shelf (WFS) in late autumn/early winter, CAO events may result in discoloration of surface waters over wide areas of the shelf that may persist for two to five days [10]. Under the hypothesis that the brightness anomaly was driven by highly reflective, inorganic sedimentary particles, as supported by examination of satellite-derived Inherent Optical Properties (IOPs), the temporal and spatial persistence of the discoloration appeared to be sustained through convective water column turbulence. Hindcast numerical simulations of the air–sea interactions indicated continuing heat losses from the ocean for the duration

of the CAO event that rendered the water column dynamically unstable precisely where sustained surface water discoloration was persistent. The combined remote sensing and numerical modeling analysis suggested that a sustained coastal brightness anomaly during a CAO event indicates continuing surface ocean heat losses and an accompanying dynamic instability that penetrates to the sea floor.

In this paper, later season CAO events (March 2018) are examined wherein the spatial and temporal extent of the ocean color brightness anomaly over the WFS is comparatively restricted. Concomitant numerical simulations of the ocean's response to CAO events in the setting of seasonal warming and increasing thermal stratification are used here to test the hypothesis that optical signals (and the manifest ocean color images) indicate where turbulent mixing consumes the water column down to the ocean bottom and when thermal stratification has reestablished hydrologic stability.

2. Materials and Methods

2.1. Ocean Color Images and Buoy Data

Satellite data were obtained from the Ocean and Land Colour Imager (OLCI) on board the Sentinel-3A/B satellites, the Visible Infrared Imaging Radiometer Suite (VIIRS) on the Suomi-National Polar-Orbiting Partnership (NPP) and NOAA-20 satellites, and the Advanced Baseline Imager (ABI) on the Geostationary Operational Environmental Satellite (GOES)—East satellite. True color images derived from OLCI and VIIRS sensor data were obtained from NOAA STAR Ocean Color Science Team Ocean Color Viewer website (OCView: https://www.star.nesdis.noaa.gov/ (accessed on 7 June 2022)) and were rendered from the intermediate surface reflectance products that may include land and clouds in the images. OLCI and VIIRS data were further processed to remove atmospheric contamination and yield surface Level-3 products (IOPs) using the Naval Research Laboratory's (NRLs) Automated Optical Processing System (AOPS) [11].

In this paper, we also examine visible band data from the geostationary GOES-ABI sensor. The ABI sensor is not intended for ocean color applications; however, some coastal ocean scenes may be rendered due to the very high reflectivity signals from suspended sediments. GOES-ABI Level 1B conus data (~500 m horizontal resolution for the 640 nm band) were obtained from the NOAA Comprehensive Large-Array Data Stewardship System (CLASS) and processed using the AOPS system to produce ocean surface reflectance fields [ρ_s] [12]. A method to convolve GOES-ABI data with dedicated ocean color sensor information is described in Jolliff et al. [13], and was used to create true color image sequences from GOES-ABI data.

Meteorological and oceanographic buoy data were obtained from NOAA's National Data Buoy Center (https://www.ndbc.noaa.gov (accessed on 6 May 2022)).

2.2. COAMPS and Sediment Models

The Coupled Ocean-Atmosphere Mesoscale Prediction System (COAMPS) is the U.S. Navy's operational two-way coupled ocean-atmosphere numerical modeling system [14–16]. The nested atmospheric and ocean models exchange information on fluxes of thermal energy and other data via the Earth System Modeling Framework (ESMF). The Navy Coastal Ocean Model (NCOM) [17] was used as the ocean model component and configured at 3 km horizontal resolution for the northern Gulf of Mexico encompassing the WFS. Initial and boundary conditions were obtained from the global application of the Hybrid Coordinate Ocean Model (HYCOM) [18]. The ocean grid consisted of 50 vertical levels, with 36 terrain-following sigma layers between the surface and 190 m depth, and 14 fixed-depth layers between 190 m and the maximum depth of 5500 m. The Navy's two-minute-resolution Digital Bathymetric Data Base (DBDB2) provided bathymetric data. The atmospheric model's inner nest was at 6 km horizontal resolution and had 60 vertical levels. Atmospheric boundary conditions for each of the forecasts were provided by the Navy Operational Global Atmospheric Prediction System (NOGAPS) model [19]. Additional details on model coupling, information exchange, and ocean-atmosphere data assimilation may be found elsewhere [20,21].

Vertical eddy diffusivities (K_v, $m^2 s^{-1}$) from the COAMPS simulations were saved at hourly increments and then interpolated to a regular vertical grid of 1 m depth increments for each model grid location over the mid- to inner-continental shelf (<60 m total depth). The diffusivities were used to solve, via implicit numerical solution, for the vertical movement of particles over a time step of 360 s. Particles were subjected to a constant sinking velocity (3.5×10^{-4} m s^{-1}) over the same time step interval. The designated sinking velocity was appropriate for very fine suspended particles in a marine environment [22–24]. The bottom-most vertical grid cell was initialized with a constant value (for the domain) of 100 g m^{-3} erodible sediment. This can also be interpreted as a percentage, and the bottom grid is at an initial 100% of the suspended particulate matter within the bottom boundary layer. A more rigorous treatment of sediment would include the resuspension process from the seafloor. However, the emphasis here is upon the surface expression of any potential particulate materials already suspended in the water column. The simulation was performed iteratively across the spatial domain as a series of one-dimensional computations. The deliberate lack of horizontal advection was intended to isolate the potential impact of vertical turbulence-driven water column overturn and the competing influence of particle settling upon the apparent optical manifestation of suspended particle scattering during the CAO events.

3. Results

3.1. Buoys and Ocean Color Sensors

The Pulaski Shoals Light (NDBC buoy PLSF1, 24.693° N, 82.773° W) is located in the extreme southern end of the WFS, and thus provides a meteorological record of southerly penetration of cold fronts, their frequency, and relative intensity. For March 2018, four episodes are evident in the meteorological record as intensified north winds (Figure 1A) and a simultaneous decline in lower air temperatures (Figure 1B). In the latter two events, lower air temperatures drop > 8 °C in less than 48 h. These are prototypical CAO events, and it is reasonable to assume that the intense north winds and the significant drop in air temperatures would have a deleterious impact on any developing upper ocean thermal stratification, despite the background seasonal trend towards increased surface ocean temperatures.
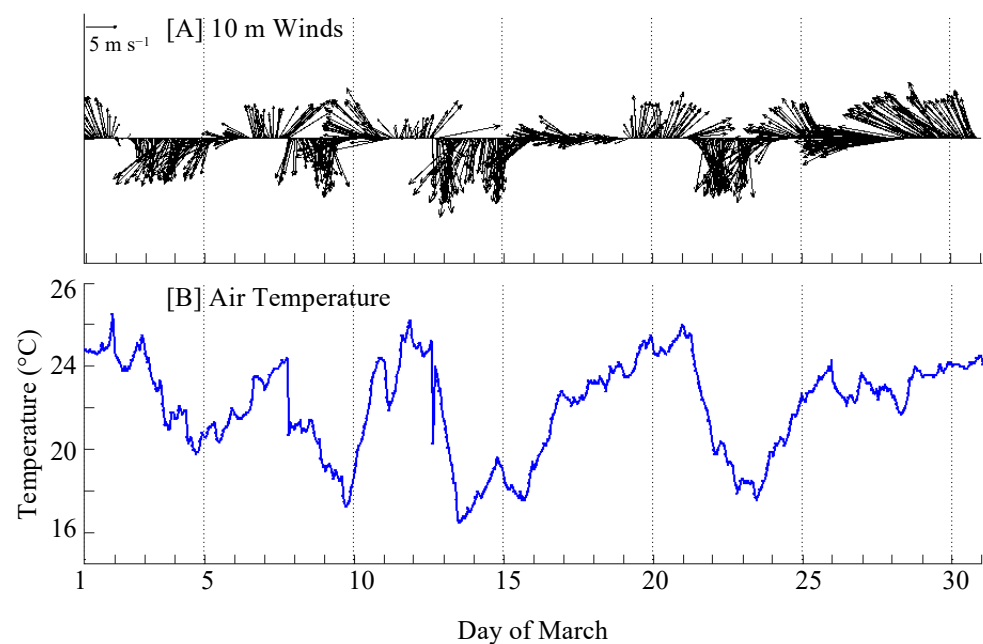
Figure 1. (**A**) 10 m wind vectors (17.1 m) PLSF1—Pulaski Shoals Light, National Data Buoy Center C-MAN Station, ARES payload, 24.693° N 82.773° W. (**B**) Air temperatures (blue line) PLSF1.

Examination of ocean true color images obtained during these CAO events reveal a concomitant discoloration of nearshore waters that is obvious when contrasted with the color signals during the interval periods. For example, a warm interval (11 March, Figure 1B) corresponds to a typical ocean color scene for the WFS and along the West Florida coastline (Figure 2A). However, as the north winds strengthen and the air temperature drops over 13–14 March (Figure 1A,B), a distinct whitish brightness in the true color images develops along the Florida coastline and over a large portion of the southern WFS (Figure 2B,C).
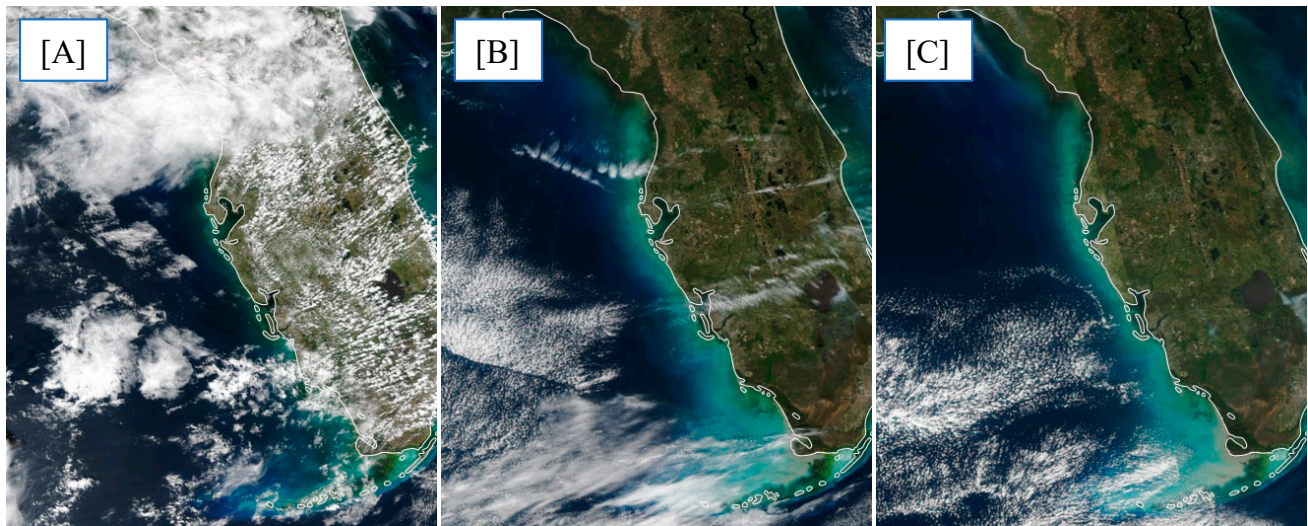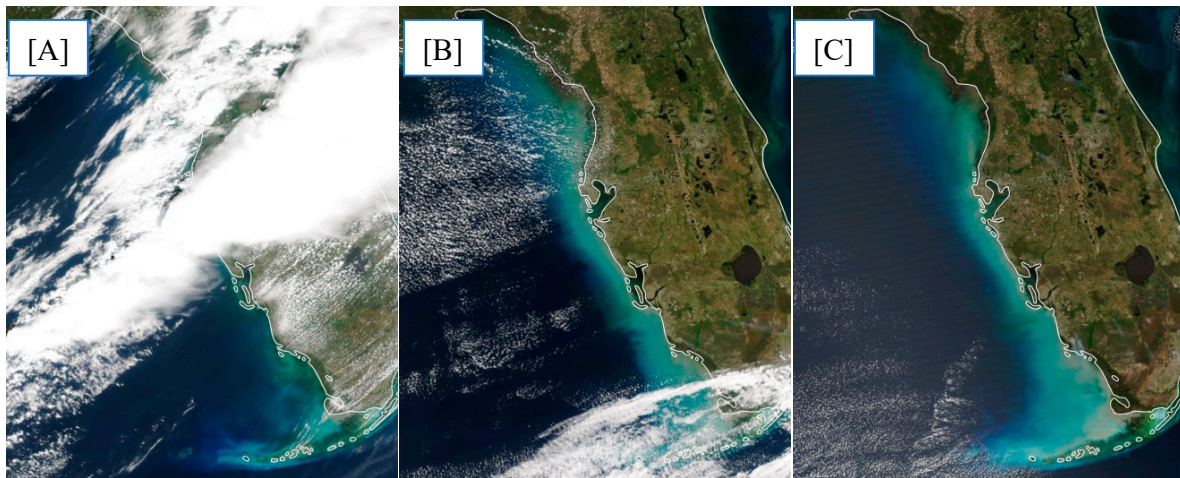

Figure 2. (**A**) VIIRS (SNPP) true color/surface reflectance, West Florida Shelf, 11 March 2018; (**B**) 13 March 2018; (**C**) 14 March 2018. Images obtained from NOAA STAR Center for Satellite Applications and Research (http://star.nesdis.noaa.gov (accessed on 7 June 2022)).

In the previously examined late autumn to early winter CAO examples, the coastal brightness anomaly extended west from the Florida coastline to the ~60 m isobathymetric contour [10]. In this case, however, the discoloration pattern extends out to approximately the ~25 m isobathymetric contour. Mid-latitude continental shelves undergo seasonal transitions from relatively well-mixed surface waters to the establishment of the seasonal thermocline [25], and in the Gulf of Mexico the seasonal thermocline is often found in the ~30 m depth range [26–28]. Thus, the apparent turbidity initiated by these late winter/early spring CAO events results in a more spatially restricted coastal pattern as the shelf water column is more dynamically stable.

The following CAO event on 21–25 March (Figure 3) reveals a similar discoloration pattern with the apparent brightness pattern extending seaward from the coastline. Note the cloud indicating the frontal boundary as it penetrates south on 20 March (Figure 3A). The brightness pattern is most conspicuous in the southern portion of the shelf, where there is a relatively shallow plateau extending along the Florida Keys (Figure 3B,C). Our prevailing hypothesis is that the discoloration is due to the vertical mixing of highly reflective particles, and the spatial extent of the discoloration is indicative of where ocean turbulence has penetrated to the seafloor. Hence, as the CAO-induced turbulence subsides and thermal stratification ensues, the particles will settle and the discoloration will recede.

The color images suggest there is both a day-to-day as well as a diurnal trend in the particle excitation/settling sequence (Figure 4). On 23 March, winds are diminishing and air temperatures begin increasing (as shown in Figure 1). Over the southern portion of the WFS, the Sentinel 3A OLCI image captured at 15:44 UTC (10:44 local, CDT) shows a brightness discoloration over much of the southwest shelf (Figure 4A). A subsequent image from VIIRS (NPP, 18:14 UTC; Figure 4B) indicates some dissipation of the brightness signal (setting aside the smoke from a nearby Everglades wildfire), and the final VIIRS image

(NOAA-20, 19:06 UTC; Figure 4C) is substantially different from the earlier OLCI image, with much of the apparent brightness pattern having faded over the intervening ~4 h.


Figure 3. (**A**) VIIRS (SNPP) true color/surface reflectance, West Florida Shelf, 20 March 2018; (**B**) 21 March 2018; (**C**) 22 March 2018. Images obtained from NOAA STAR Center for Satellite Applications and Research (http://star.nesdis.noaa.gov (accessed on 7 June 2022)).
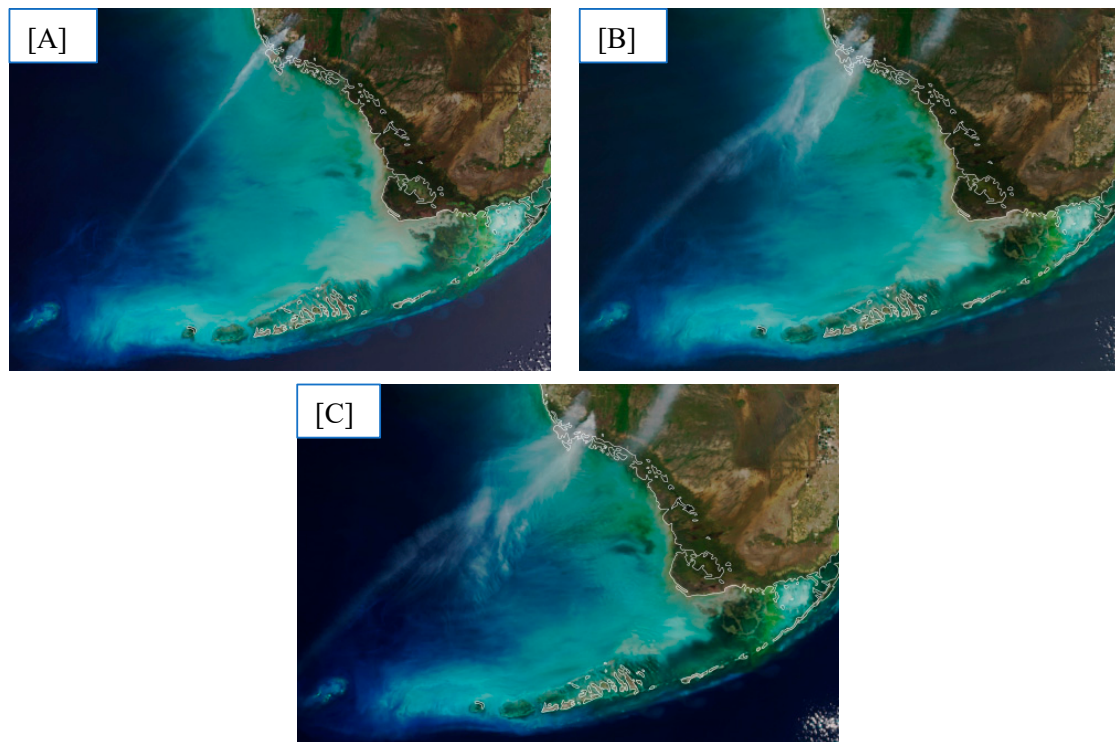
Figure 4. True color images obtained on 23 March 2018 over the southern portion of the WFS: (**A**) OLCI Sentinel A, 15:44 UTC; (**B**) VIIRS SNPP, 18:14 UTC; (**C**) VIIRS NOAA-20, 19:06 UTC. Images were obtained from NOAA STAR Center for Satellite Applications and Research (http://star.nesdis.noaa.gov (accessed on 7 June 2022)).

The potential inferences made from surface reflectance-based true color images are further supported by the level-3, fully processed surface optical properties. The Quasi-Analytic Algorithm (QAA) [29] total backscattering coefficient is an appropriate potential indicator of elevated particle backscattering. There is a significant contrast between the OLCI backscattering field (Figure 5A), captured at 15:44 UTC, and the NOAA-20 VIIRS

product (Figure 5B; 19:06 UTC). In both fields, smoke from the nearby wildfire prevents processing beneath the atmospheric contamination. In the OLCI product field, additional atmospheric correction failure prevented product retrievals farther west. However, enough information was retrieved to show, in cross-shelf transect, an apparent elevation in backscattering values along ~25.15° N latitude in the OLCI products (Figure 5C) compared to the VIIRS products retrieved ~4 h later. This pattern in the retrieved level-3 optical products suggests a potential diurnal cycle of turbidity excitation and relaxation that was suggested in the true color images (Figure 4).
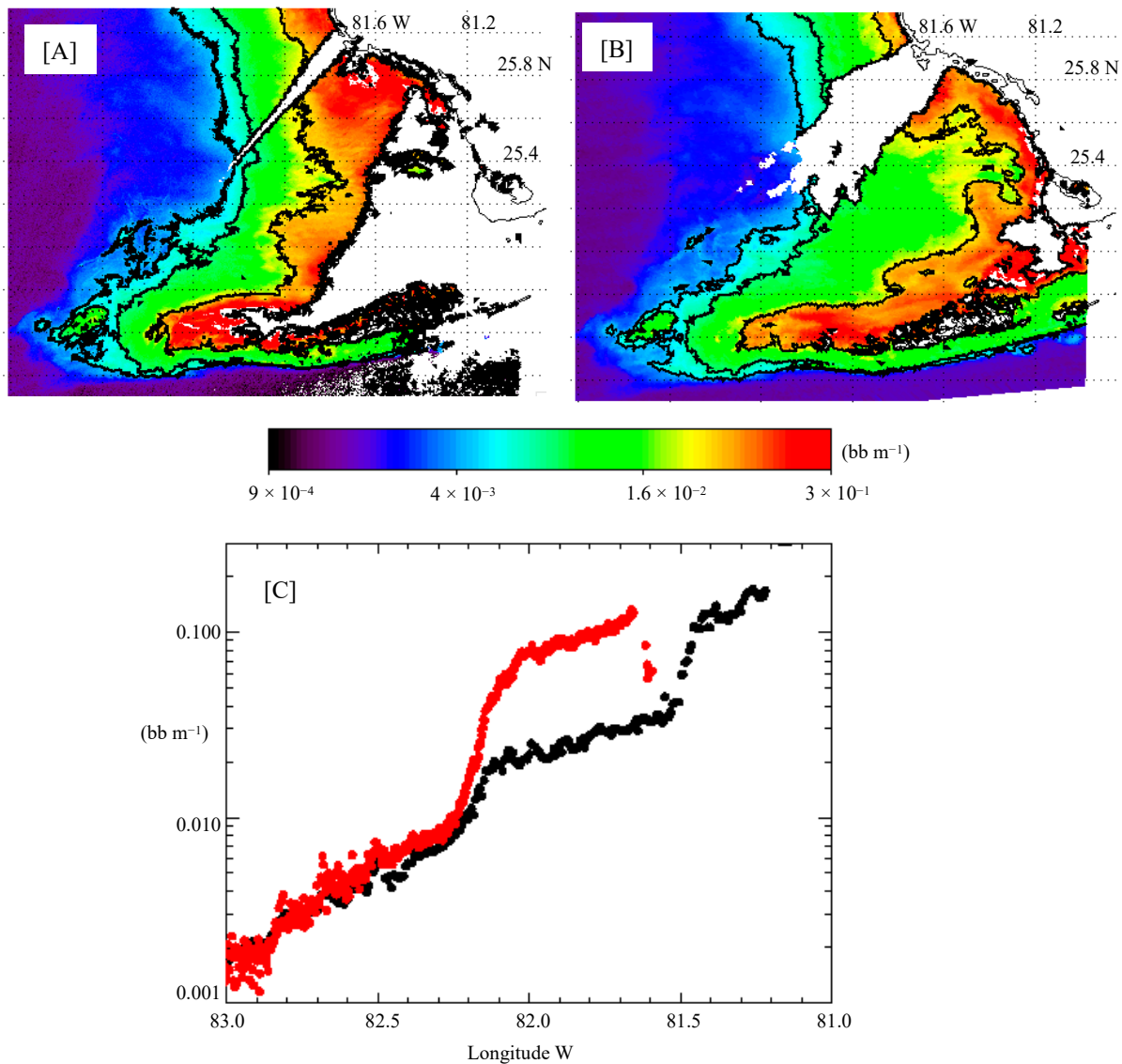
Figure 5. (**A**) QAA backscattering coefficient (560 nm) level-3 product, OLCI Sentinel 3A, 23 March 2018, 15:44 UTC; (**B**) QAA backscattering coefficient (555 nm) level-3 product, VIIRS NOAA-20, 23 March 2018, 19:06 UTC; (**C**) comparison of products shown in (**A**,**B**) along 25.15° N latitude, (OLCI-red, VIIRS-black).

The optical property product fields also suggest a pattern of an initial disturbance, the CAO event, which leads to turbidity in the water column that is progressively diminished over a period of days (Figure 6). The backscattering coefficient products obtained from the same sensor (VIIRS, NOAA-20) appear to diminish in magnitude over the southern shelf area from a maximum on 22 March (Figure 6A), through a progressively diminishing signal intensity (Figure 6B,C), arriving at much lower values on 25 March (Figure 6D).

Simultaneously, there is also an apparent diurnal pattern that suggests particles are settling as daily warming ensues and thermal stratification begins to reestablish.
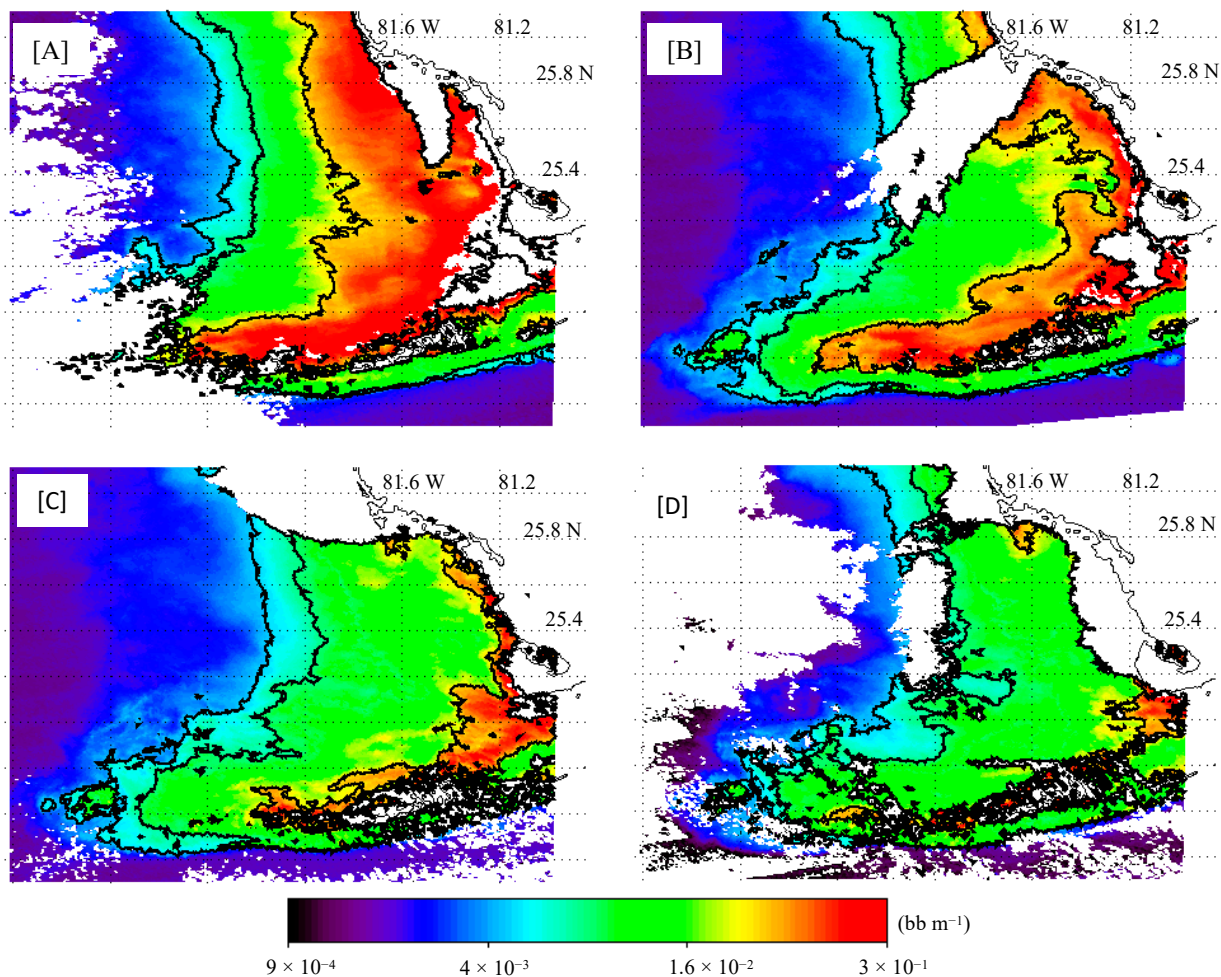

Figure 6. QAA backscattering coefficient (555 nm) level-3 product fields from NOAA-20 VIIRS for (**A**) 22 March, 17:44 UTC; (**B**) 23 March, 19:06 UTC; (**C**) 24 March, 18:47 UTC; (**D**) 25 March, 18:28 UTC.

3.2. COAMPS Results

Overall patterns seen in the color satellite images appear consistent with the ocean model results from COAMPS. Simulated lower air and upper ocean temperatures for a central point on the southern portion of the WFS (25.21° N, 81.56° W,) are indicative of alternating conditions between CAO outbreaks and seasonal warming during March (Figure 7). For example, as simulated air temperatures drop on 21 March (Figure 7A), the air–sea temperature difference approaches −4 °C (Figure 7B). The temperature difference is indicative of an ensuing period of elevated heat losses from the ocean to the atmosphere. Air temperatures then rapidly increase on 23 March as the air–sea temperature difference diminishes. Simulated sea surface temperatures diminish from 22 to 24 March, and then increase thereafter.

Simulated water column temperatures indicate repeated cycles of surface warming, water column mixing, and ocean cooling during the same period (Figure 8). The mid-March CAO event (13–17) leaves the water column in the 21–22 °C range, but surface warming ensues as the CAO event recedes. Evidence of surface warming resumes on 19 March and extends into 21 March (Figure 8) with surface waters > 23 °C. However, as the initial onset phase of the next CAO event begins at midday on 21 March, the diurnal surface warming is mixed down into the water column as the upper water column thermal stratification pattern is destroyed. The ocean then enters a period of heat loss for the next few days,

and water temperatures descend back into the 21–22 °C range. A return to diurnal surface warming becomes more prominent on 25 and 26 March (Figure 8).
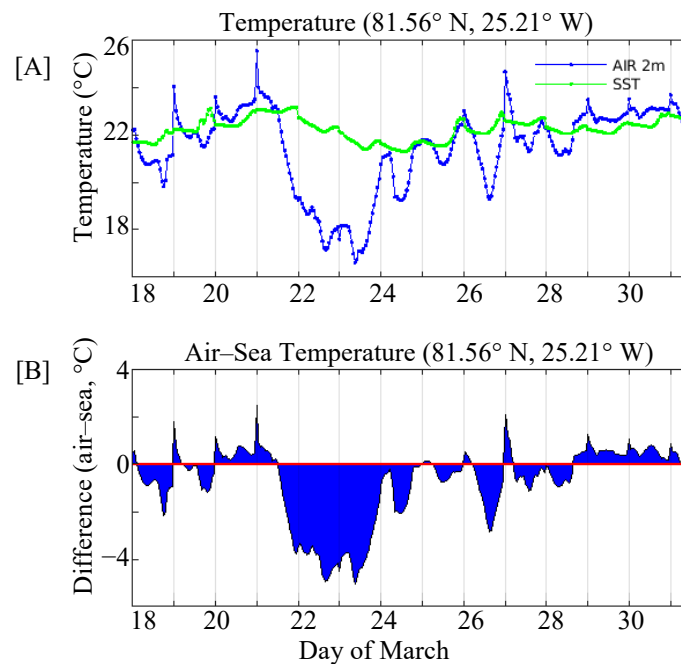

Figure 7. (**A**) COAMPS simulated air temperatures at 2 m height (blue line) and simulated sea surface temperature (SST) (green line); (**B**) temperature difference (2 m air temperature—SST). The blue area highlights the air–sea temperature difference, and the red line is the zero air–sea difference line.
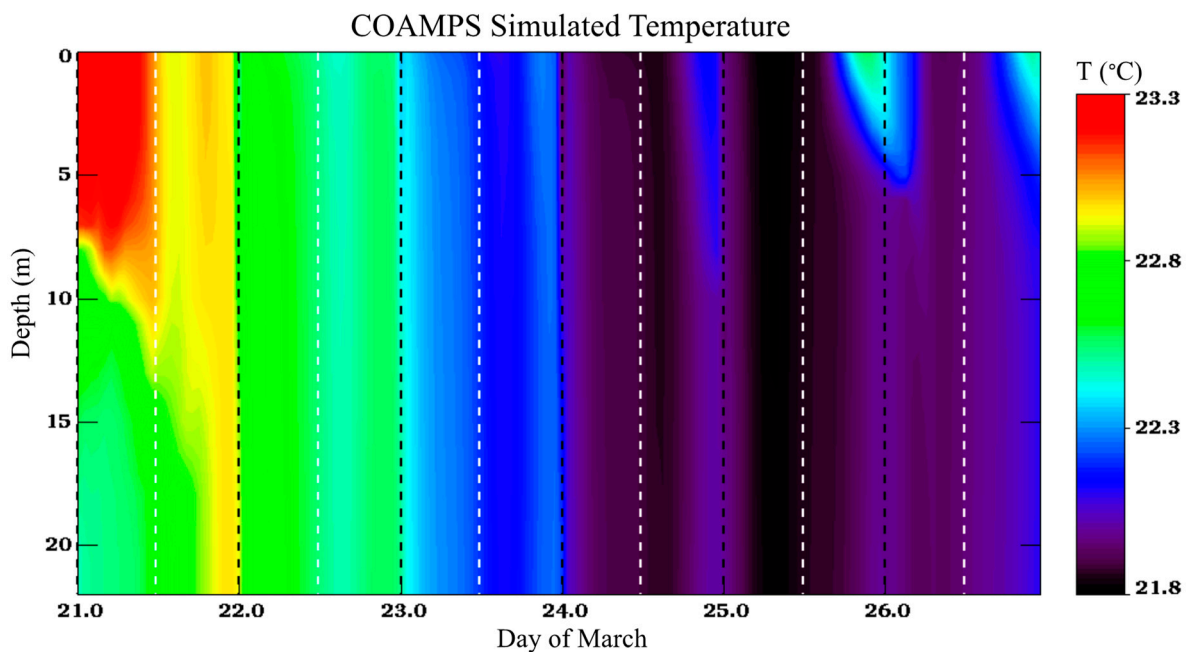
Figure 8. Simulated water column temperatures for 25.15° N, 82.20° W, from 21 to 27 March 2018. White dashed lines indicate the approximate local time for sunrise and the black dashed lines are for local sunset.

The model's estimate of the vertical eddy diffusivity coefficient (K_v, m^2 s^{-1}; based on the Mellor–Yamada turbulence closure scheme [30]) at the same location is informative about the simulated cycle of mixing and stratification, and how it is disrupted by the CAO event (Figure 9). Vertical eddy diffusivities become maximal throughout the water column

at the end of 21 March, and then maintain these elevated values (~9 × 10^{-2} m^2 s^{-1}) that are progressively disrupted by a diurnal relaxation pattern. Note that K_v values of order 10^{-2} (red areas in the contour plot) imply vigorous, rapid mixing for a water column of only 22 m depth. The mixing pattern with a diurnal relaxation (indicated by lower K_v values following sunrise, dashed white line in Figure 9) becomes more obvious on 23 March, and becomes progressively larger thereafter. Progressively reduced periods of vigorous water column mixing each day following 22 March would be consistent with the inference of vertical particle movements inferred from the ocean color products (Figures 5 and 6).
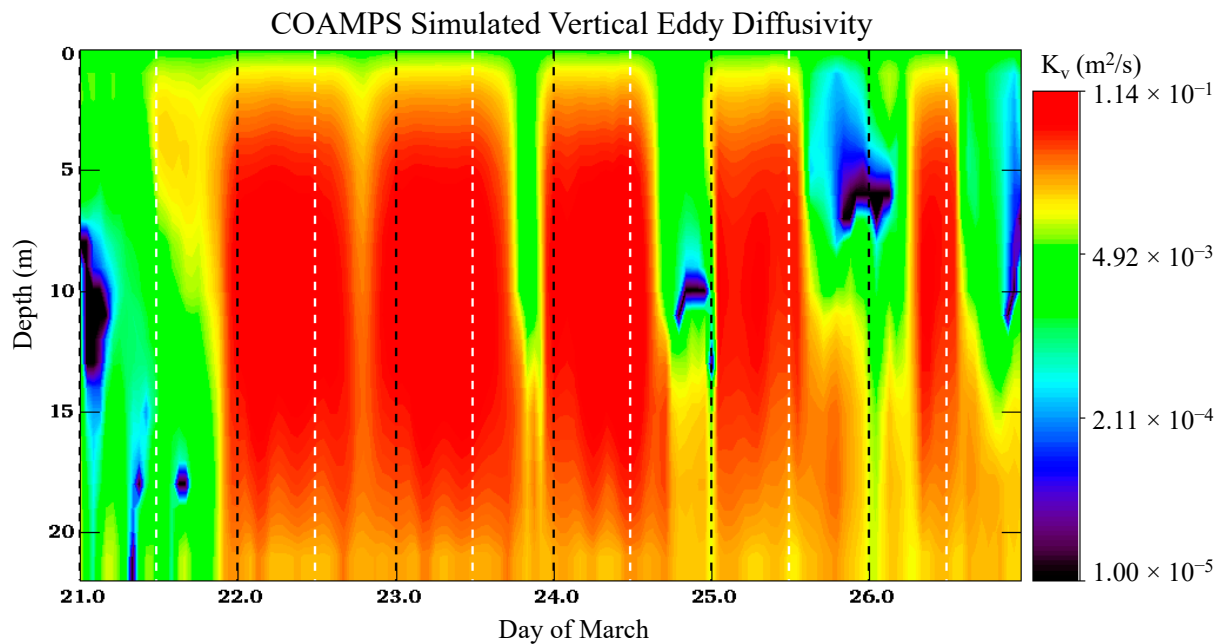
Figure 9. COAMPS results for water column vertical eddy diffusivity for 25.15° N, 82.20° W, from 21 to 27 March. White dashed lines indicate the approximate local time for sunrise and the black dashed lines are for local sunset.

The eddy diffusivity results are also consistent with the COAMPS simulated surface air–sea fluxes. Net surface heat fluxes are positive during the day (surface warming) and negative during the night (surface cooling; Figure 10). However, the 24 h smoothed net flux (dashed line Figure 10) indicates a net heat loss from the ocean during the CAO event from 21 to 24 March (Figure 10). The smoothed air–sea flux trend is consistent with the SST pattern in Figure 9. The length of time each day during which net heat flux is positive also increases during that time interval, corresponding to reduced intervals of vertical mixing.

In summary, the COAMPS air–sea simulation corroborates the inferences made from the buoy data and the ocean color image sequence: the CAO event destroys the developing thermal stratification along the coasts and significant heat losses induce mixing (overturn) of the water column. Consistent with our hypothesis, this process has the potential to bring near-bottom sediments to the surface and result in the brightness anomaly seen in reflectance-based true color images as well as the elevated backscattering coefficients in the level-3 IOP product fields. As the CAO event wanes, the diurnal cycle of heating and cooling tips towards the balance of net heating over a 24 h period, and vertical mixing is curtailed as thermal stratification is restored. For the flux of resuspended particles that may contribute to the observed surface water discoloration, the return of stratification results in their settling to the ocean bottom or near-bottom turbidity layers. This would potentially explain the color discrepancy seen in ocean color reflectance images separated by mere hours on 23 March (see in Figure 4).
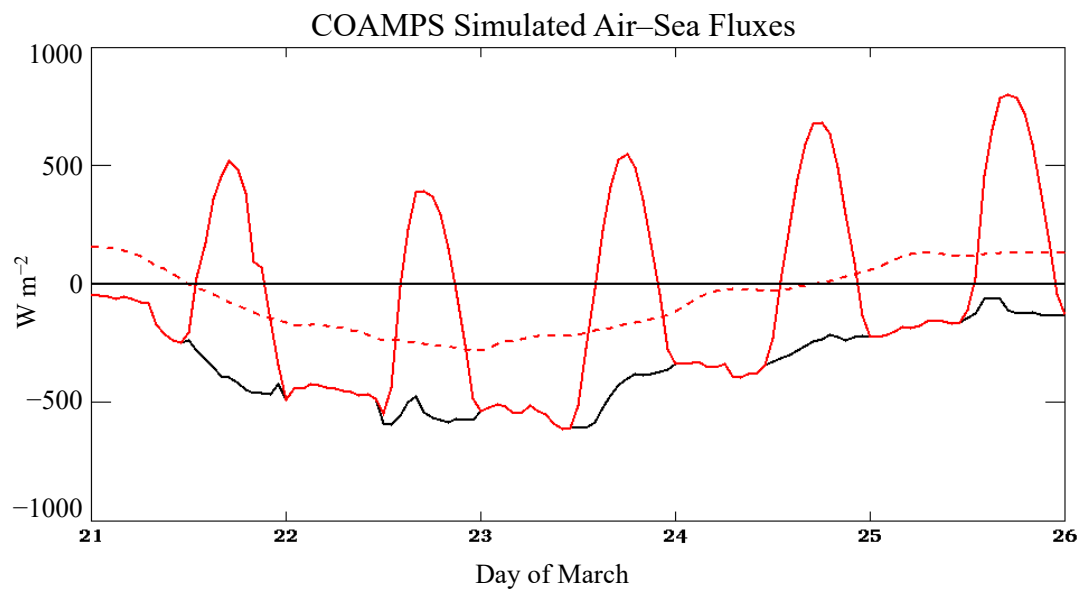
Figure 10. Simulated air–sea heat fluxes for the location 82.20° W and 25.15° N, as in Figures 8 and 9. Solid red line is the total heat flux, the black line is the turbulent and longwave fluxes, and the dashed red line is the 24 h smoothed total flux.

3.3. GOES-R Image Sequences

GOES-R ABI image sequences were available for the period of hours depicted in the dedicated ocean color sensor frames shown in Figure 4. The surface reflectance (ρ_s) product for the ABI red band (centered at 640 nm) is a useful proxy indicator of suspended sediment because variance in the red band for other radiometers has been used to develop algorithms for surface suspended sediment concentration [31,32]. Scaling of ρ_s-640 may be used as a qualitative indicator of surface sediment concentration in ocean areas. The sequence of ABI images (Figure 11) corroborates the ocean color sequence: beginning at 15:30 in the southern section of shelf, the apparent sediment signal begins to diminish. Nearly 150 min later, the reflectance signal has substantially diminished (18:02 UTC, Figure 11).

**GOES ABI Red Band Surface Reflectance 23 March 2018**
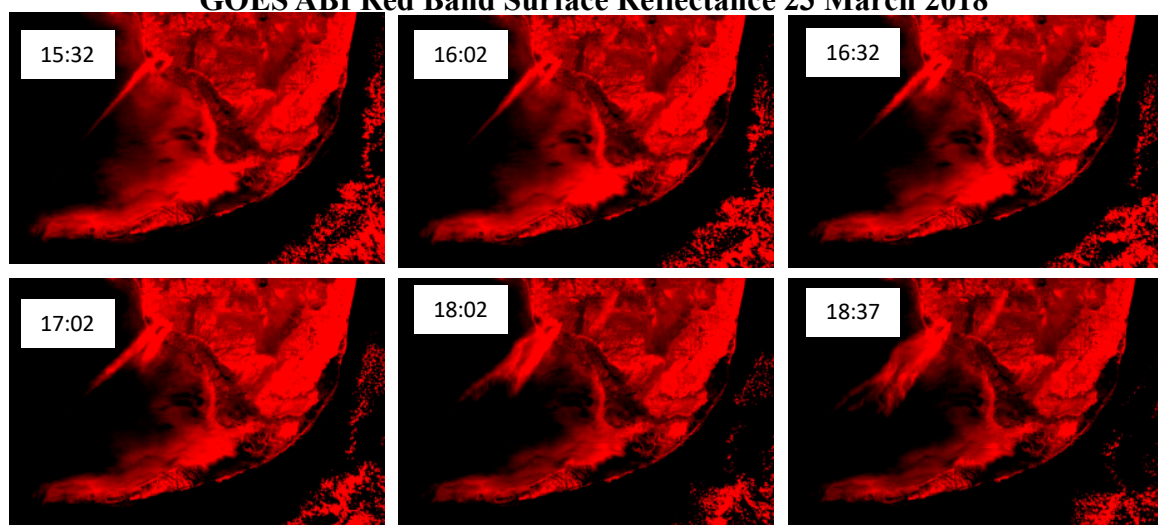
Figure 11. Red band surface reflectance from GOES-R ABI on 23 March 2018, times (UTC) are indicated in each respective panel.

Geostationary satellite image brightness may vary throughout the daily sequence due to bidirectional reflectance distribution function (BRDF) artifacts [33–35], and this is

a consequence of the changing geometry between the sensor viewing angle and the solar illumination angle. To identify potential BRDF contamination in the image, the reflectance values were normalized by the 15:32 red band signal on 23 March (Figure 12). In panel 18:37 (Figure 12D), diminished brightness over land indicated some BRDF impacts on brightness due to the changing sun-to-target-to-sensor geometry. However, brightness values for the entire scene generally increase with increasing solar zenith angle (overhead at 0° and the horizon at 90° for convention), and the contrast between the normalized reflectance images for 16:02 and 18:37 over the shelf suggest a diminished signal beyond any BRDF impacts.

GOES ABI Red Band Normalized Surface Reflectance 23 March 2018
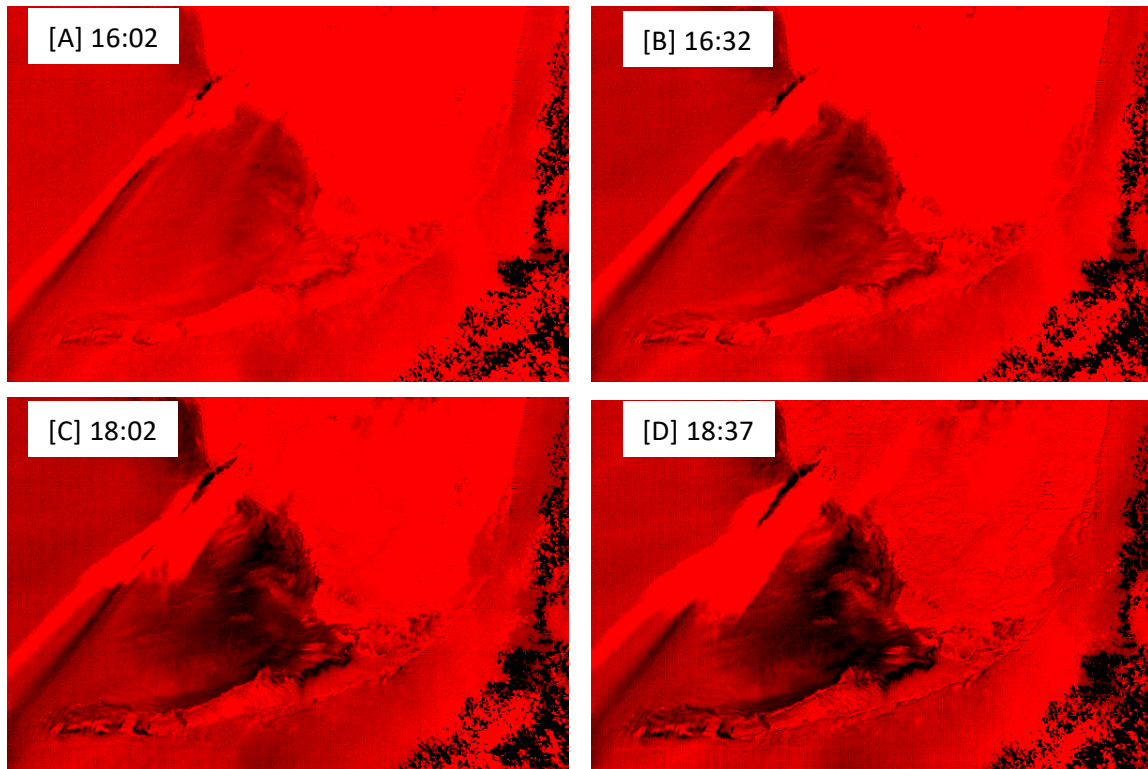
Figure 12. GOES-R (ABI) band 2 (640 nm) surface reflectance normalized by the reflectance values obtained on image 15:32 on 23 March; displayed times (UTC) are (**A**) 16:02, (**B**) 16:32, (**C**) 18:02, and (**D**) 18:37.

The color-enhanced GOES-R images, based upon surface reflectance (Figure 13), indicate a diminished color brightness signature that is not commensurate with changes in other features that appear in the sequence. Both the ABI blue and red reflectance data show a diminishing signal over the shelf that is consistent with the multi-sensor true color comparison on 23 March and the backscattering product comparison on the same date (Figures 4 and 5). The image sequence, at ~5 min intervals, confirms the change in brightness is occurring within 4 h between 11:00 and 16:00 local time. An animation of the GOES color-enhanced sequence for this time period is provided in the Supplementary Materials. This interval corresponds to the interval of simulated positive heat flux (Figure 10), and reduced vertical eddy diffusivity (Figure 9). Thus, a relaxation of vertical mixing corresponds to (1) a change in air–sea heat flux from negative to positive, and (2) a potential dominance of particle settling that may result in a reduced apparent brightness pattern in ocean color images. This hypothesis is tested in the following section with an explicit sediment mixing/settling numerical model.

**GOES ABI Color Enhanced Images 23 March 2018**
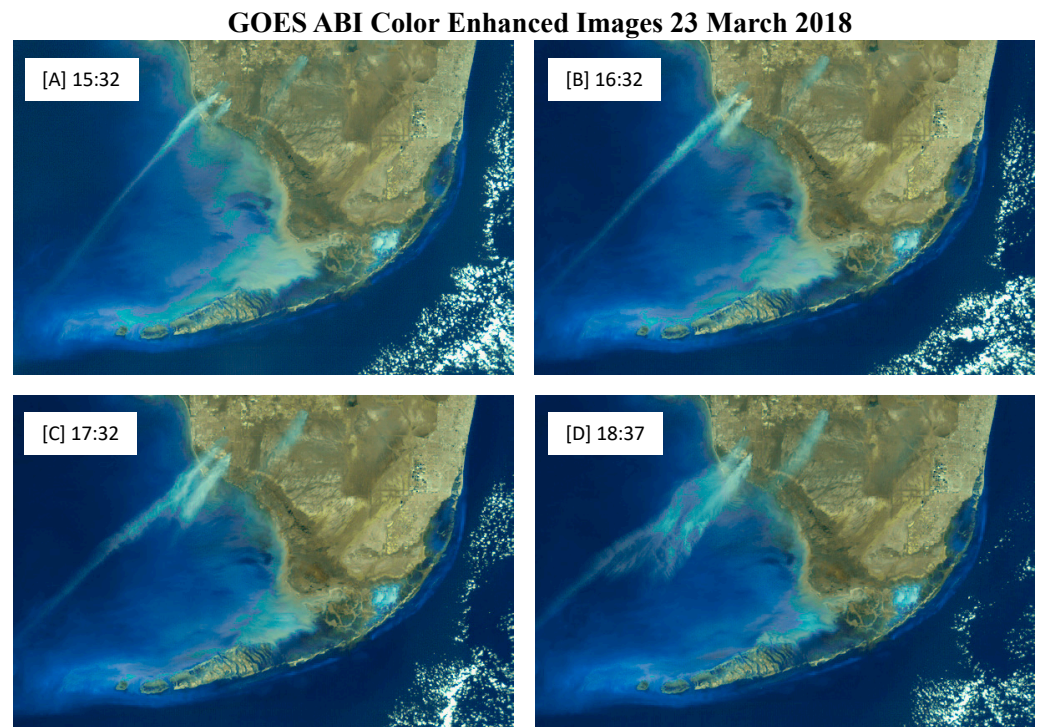
Figure 13. Color-enhanced image sequence on 23 March 2018 from GOES-R ABI. The color-enhancement technique takes information from both ABI band 1 (470 nm) and band 2 (640 nm) to generate a true color reflectance image, using an estimated value for the green reflectance; times (UTC) shown are (**A**) 15:32, (**B**) 16:32, (**C**) 17:32, and (**D**) 18:37. An animation of the entire sequence is provided in the Supplementary Materials.
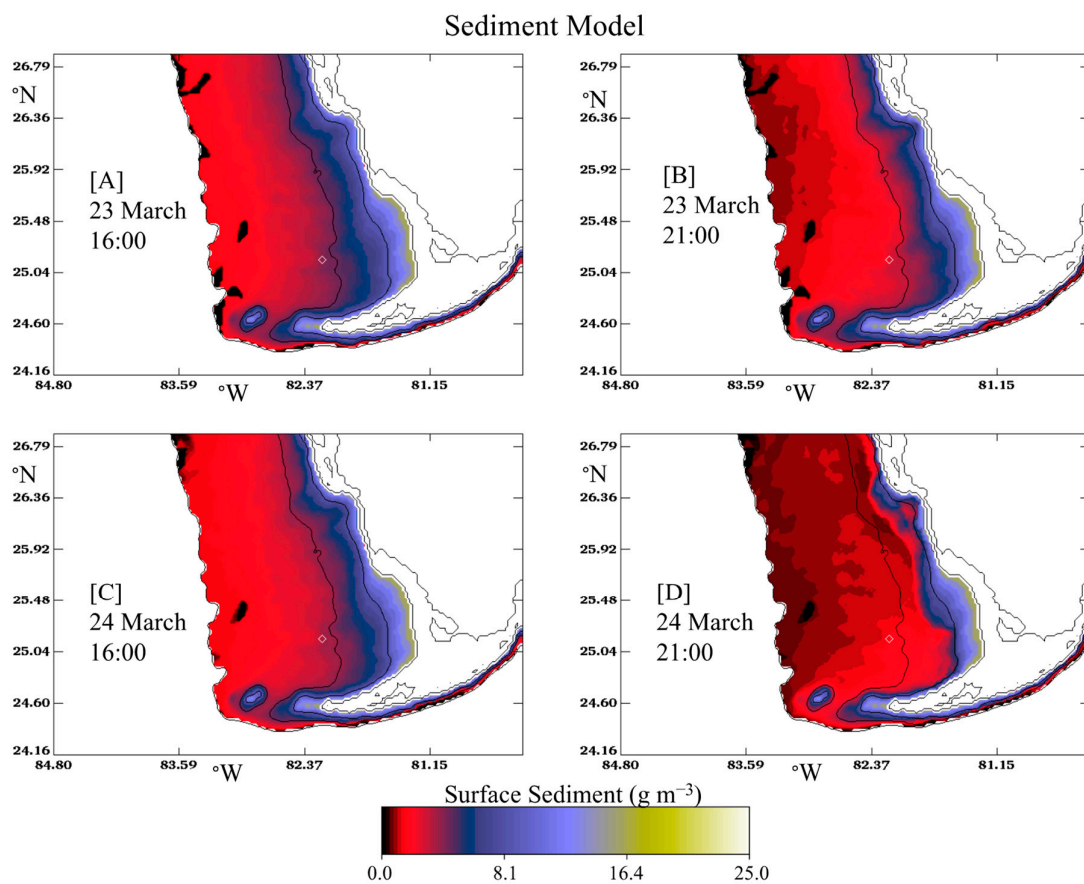
3.4. Sediment Model

Results from the sediment model, driven by simulated vertical eddy diffusivities from COAMPS and a constant settling velocity, mimic patterns seen in the ocean color images (Figure 14). Surface expression of potential resuspended sediments is not evident until the CAO event late on 21 March. Thereafter, settling briefly interrupts the vigorous mixing during diurnal warming for progressively larger intervals, consistent with the patterns seen in the vertical diffusivities (Figure 9) and the surface heat fluxes (Figure 10). This pattern can be seen in the surface sediment results as well (Figure 14). On 22 March, there is a slight diminishment in the surface sediment concentration during daylight hours (to the right of the white dashed line in Figure 14). On 23 March, there is a comparatively increased interval of diminished surface sediment at 21:00 UTC compared to 16:00 UTC (16:00 and 11:00 local, CDT). Since we initialize the bottom layer at a value of 100, the surface expression can be also considered a percent of the erodible materials from near-bottom. The following day, 24 March, the diurnal collapse of the surface sediment expression is even more pronounced (Figure 14), and the diurnal interval enlarges over the following two days (25 and 26 March, Figure 14).

The pattern shown for the water column may be visualized over the larger shelf region (Figure 15). Each day forward from 22 March, the diurnal interval of reduced mixing and net surface ocean warming results in less potential for the surface expression of near-bottom sediments. The model suggests a diurnal pattern where surface warming leads to diminished mixing and diminished surface sediments as sinking becomes the dominant term in the sediment model. The contrast becomes evident between 16:00 and 21:00 UTC time, and mimics the diurnal patterns shown earlier (Figures 4, 5 and 13). The sediment model also reproduces the day-to-day diminished reflectance signal onward from 22 March. As the period of diurnal warming increases and intensifies, so surface sediment expression is progressively diminished. Finally, on 25 March, the surface expression of sediment appears to collapse in the afternoon simulation (Figure 16).

Simulated Suspended Sediment
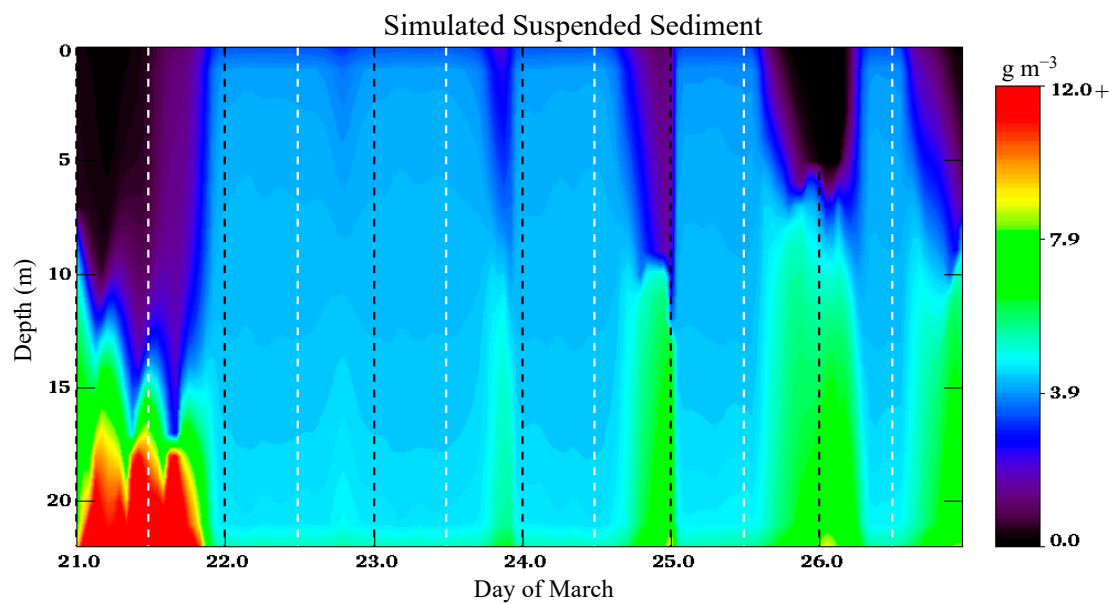
Figure 14. Results from the sediment model showing the concentration of sediment (g m^{-3}) in the water column for the location 25.15° N and 82.20° W, as in Figures 8–10. White dashed lines indicate the approximate local time for sunrise and the black dashed lines are for local sunset. High values in the lower left-hand corner of the plot saturate to a maximum value of 23.3 g m^{-3}.

Sediment Model

Figure 15. Results from the sediment model. Surface sediment concentrations (g m^{-3}) (or percent of bottom boundary initial condition) are mapped for the surface distribution (2 m) for (**A**) 23 March 16:00 UTC, (**B**) 23 March 21:00 UTC, (**C**) 24 March 16:00 UTC, and (**D**) 24 March 21:00 UTC. The white triangle indicates the position for Figures 8–10 and 14.
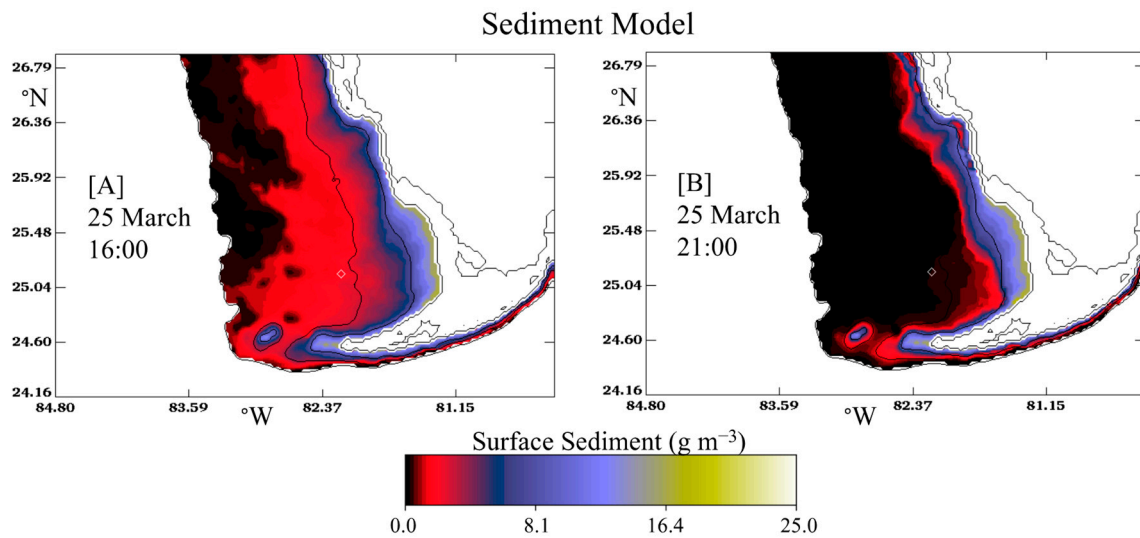
Figure 16. Results from the sediment model. Surface sediment concentrations (g m^{-3}) (or percent of bottom boundary initial condition) are mapped for the surface distribution (2 m) for (**A**) 25 March 16:00 UTC, and (**B**) 25 March 21:00 UTC. The white triangle indicates the position for Figures 8–10 and 14.

4. Discussion

During boreal late winter and early spring, the WFS undergoes a seasonal transition from wintertime well-mixed shelf waters to summertime thermal stratification [36–38]. CAO events nonetheless persist into this transitional period [39,40], though the impact of the wind stress and ensuing heat losses manifest differently in both the physical and optical characteristics of the shelf. In the spring transitional period, heat losses appear not to overturn the water column over as wide a shelf area as during earlier in the year and the brightness anomaly seen in the ocean color images is more restricted to shallower depths. A salient feature of the spring transition is the formation of a seasonal thermocline due to reduced winds and increased surface heating [41,42], and in the Gulf of Mexico, the seasonal thermocline forms at ~30 m depth [43]. Thus, CAO events during this transitional period appear as a fluctuation (heat loss event) during conditions trending in the opposite direction (a warming ocean) [44]. The spatial extent and duration of sustained heat losses from the surface ocean appear to correspond to the model's estimates of vertical eddy diffusivities, and these, in turn, correspond to brightness patterns seen in ocean color images. Thus, our hypothesis is that the ocean color pattern is likely indicative of where vertical overturn has penetrated to the seafloor. Moreover, the dissipation of the brightness signal may be indicative of where heat losses have diminished and vertical stability is being reestablished.

A number of simplifying assumptions were made during the performance of this analysis. First and foremost, the focus herein has been on a singular aspect of a very complex optical environment that manifests as radiant signals detected via satellite. Phytoplankton population dynamics [45], chromophoric detrital materials [46], and river/estuarine effluent [47] are making material contributions to the total IOPs and the resulting water-leaving radiance signals [48]. Moreover, in very shallow areas (<~10 m depth), the satellite may indeed be detecting the ocean bottom [49], which may be covered in sea grasses [50] or carbonate sands [51,52]. Nonetheless, our hypothesis is that the very high reflectivity signals are due to the transient manifestation of marine sediments that are additive, or superimposed, upon the background optical signals. A comparatively simple model of sediment mixing and settling appears to capture the diurnal to weekly patterns seen in the ocean color images.

The presumption of a vertical dominance for sediment dynamics, and the discussion of it in an entirely one-dimensional context across the shelf, is overly simplistic, but deliberately so. Northerly winds during the CAO outbreak along the West Florida coastline

are upwelling favorable [53–55] and will stimulate cross-shelf advection of near-bottom materials towards the shoreline [56]. Moreover, an excited sea state will induce vertical mixing through Langmuir circulation [56,57], as well as near-bottom wave orbital velocities and stress radiation gradients in shallower areas of the shelf [58,59]. In this paper, these additional processes were omitted from the numerical sediment simulations that nonetheless were able to mimic diurnal patterns (Figure 14) apparent in ocean color images (Figure 4) and products (Figure 5). This suggests that, to first order, the brightness anomaly in the ocean color images is an approximate indicator of water column stability over the shelf.

The particle composition, variable size distributions, optical properties, and the dynamics of sediment mobilization from the seafloor are also aspects of this integrated physical-optical-geochemical phenomenon that are beyond the scope of this paper. Here, the correspondence between the simulated mixing and settling tendencies, the air–sea flux changes, and the spatiotemporal patterns seen in satellite image sequences, provide a mechanistic framework for understanding this process. Specifically, the color brightness pattern and its subsequent dissipation in time closely aligns with changes in the surface heat flux and the resulting impact on vertical water column stability. A more detailed analysis will require in situ observations during a CAO event that include collocated optical and physical observations.

Author Contributions: Conceptualization, J.K.J.; methodology, J.K.J., S.L., T.A.S., S.A., A.L., S.M. and M.D.L.; software, J.K.J., M.D.L., S.L., A.L. and S.A.; formal analysis, J.K.J., M.D.L., T.A.S., E.J., S.L. and T.A.S.; investigation, J.K.J., S.L., M.D.L., S.A., T.A.S., A.L. and E.J.; resources, J.K.J.; data curation, J.K.J., T.A.S., A.L. and S.L.; writing—original draft preparation, J.K.J., S.L., E.J. and T.A.S.; writing—review and editing, J.K.J., T.A.S., E.J., S.A., S.L., A.L. and S.M.; visualization, J.K.J., S.A., A.L., M.D.L. and S.M.; supervision, J.K.J.; project administration, J.K.J.; funding acquisition, J.K.J. All authors have read and agreed to the published version of the manuscript.

Institutional Review Board Statement: Not applicable.

Informed Consent Statement: Not applicable.

Data Availability Statement: Satellite data used in this study are available via NASA (https://oceancolor.gsfc.nasa.gov) and NOAA (here: https://www.avl.class.noaa.gov/saa/products/welcome, and here: https://www.star.nesdis.noaa.gov/ (accessed on 7 June 2022)). Buoy data is available via the NOAA-NDBC (https://www.ndbc.noaa.gov (accessed on 6 May 2022)).

Conflicts of Interest: The authors declare no conflict of interest.

References

1. Nowlin, W.D.; Parker, C.A. Effects of a Cold-Air Outbreak on Shelf Waters of the Gulf of Mexico. *J. Phys. Oceanogr.* **1974**, *4*, 467–486. [CrossRef]
2. Villanueva, E.E.; Mendoza, V.M.; Adem, J. Sea surface temperature and mixed layer depth changes due to cold-air outbreak in the Gulf of Mexico. *Atmosfera* **2010**, *23*, 325–346.
3. Schroeder, W.W.; Huh, O.K.; Rouse, L.J.; Wiseman, W.J. SAtellite Observations of the Circulation East of the Mississippi Delta: Cold-Air Outbreak Conditions. *Remote Sens. Environ.* **1985**, *18*, 49–58. [CrossRef]
4. Dagg, M.J. Physical and biological responses to the passage of a winter storm in the coastal and inner shelf waters of the northern Gulf of Mexico. *Cont. Shelf Res.* **1988**, *8*, 167–178. [CrossRef]
5. Zavala-Hidalgo, J.; Morey, S.L.; O'Brien, J.J. Seasonal circulation on the western shelf of the Gulf of Mexico using a high-resolution numerical model. *J. Geophys. Res.* **2003**, *108*, 3389. [CrossRef]
6. DiMego, G.J.; Bosart, L.F.; Endersen, G.W. An examination of the frequency and mean conditions surrounding frontal incursions into the Gulf of Mexico and Caribbean Sea. *Mon. Weather Rev.* **1976**, *104*, 709–718. [CrossRef]
7. Huh, O.K.; Rouse Jr, L.J.; Walker, N.D. Cold air outbreaks over the northwest Florida continental shelf: Heat flux processes and hydrographic changes. *J. Geophys. Res. Ocean.* **1984**, *89*, 717–726. [CrossRef]

8. Perez, E.P.; Magana, V.; Caetano, E.; Kusunoki, S. Cold surge activity over the Gulf of Mexico in a warmer climate. *Front. Earth Sci.* **2014**, *2*, 19.

9. Hunniford, R. The Impact of Marine Cold-Air Outbreaks on the Rate of Oceanic Heat Storage in the Gulf of Mexico. Master's Thesis, Florida State University, Tallahassee, FL, USA, 2011.

10. Jolliff, J.K.; Ladner, S.; Smith, T.A.; Anderson, S.; Lewis, M.D.; McCarthy, S.C.; Crout, R.L.; Jarosz, E.; Lawson, A. On the Potential Optical Signature of Convective Turbulence over the West Florida Shelf. *Remote Sens.* **2021**, *13*, 619. [CrossRef]

11. Ladner, S.; Crout, R.; Lawson, A.; Wood, C.; Martinolich, P.M. *Validation Test Report for the Automated Optical Processing System (AOPS) Version 19*; NRL Technical Memorandum Report; NRL/MR/7331-09-9959; U.S. Naval Research Laboratory: Washington, DC, USA, 2020; p. 64.

12. Lewis, M.D.; Jolliff, J.K.; Ladner, S.; Martinolich, P. Delineation of suspended solids in river outflow from Hurricane Florence using GOES-16 ABI data. In Proceedings of the SPIE, Ocean Sensing and Monitoring XI, Baltimore, MD, USA, 14–18 April 2019; Volume 11014.

13. Jolliff, J.K.; Lewis, D.M.; Ladner, S.; Crout, L.R. Observing the Ocean Submesoscale with Enhanced-Color GOES-ABI Visible Band Data. *Sensors* **2019**, *19*, 3900. [CrossRef]

14. Hodur, R.M. The Naval Research Laboratory's Coupled Ocean/Atmosphere Mesoscale Prediction System (COAMPS). *Mon. Weather Rev.* **1997**, *125*, 1414–1430. [CrossRef]

15. Barron, C.N.; Kara, A.B.; Hurlburt, H.E.; Rowley, C.; Smedstad, L.F. Sea surface height predictions from the Global Navy Coastal Ocean Model (NCOM) during 1998–2001. *J. Atmos. Ocean. Technol.* **2004**, *21*, 1876–1894. [CrossRef]

16. Small, R.J.; Carniel, S.; Campbell, T.; Teixeira, J.; Allard, R. The response of the Ligurian and Tyrrhenian Seas to a summer Mistral event: A coupled atmosphere–ocean approach. *Ocean Model.* **2012**, *48*, 30–44. [CrossRef]

17. Martin, P.J. *Description of the Navy Coastal Ocean Model 1.0*; NRL Technical Memorandum Report; NRL/FR/7322-00-9962; Naval Research Laboratory: Washington, DC, USA, 2000; p. 45.

18. Metzger, E.J.; Hurlburt, H.E.; Wallcraft, A.J.; Shriver, J.F.; Smedstad, L.F.; Smedstad, O.M.; Thoppil, P.; Franklin, D.S. *Validation Test Report for the Global Ocean Prediction System 3.0-1/12 Degree HYCOM/NCODA: Phase I*; NRL Technical Memorandum Report; NRL/MR/7320—08-9148; Naval Research Lab: Washington, DC, USA, 2008. Available online: https://www.hycom.org/attachments/366_HYCOM-NCODA_VTR_I_Memo_Report_9148.pdf (accessed on 4 January 2022).

19. Rosmond, T.E.; Teixeira, J.; Peng, M.; Hogan, T.F.; Pauley, R. Navy Operational Global Atmospheric Prediction System (NOGAPS): Forcing for Ocean Models. *Oceanography* **2002**, *15*, 99–108. [CrossRef]

20. Chen, S.; Campbell, T.J.; Jin, H.; Gabersek, A.; Hodur, R.M.; Martin, P.J. Effect of two-way air-sea coupling in high and low wind speed regimes. *Mon. Weather Rev.* **2010**, *138*, 3579–3602. [CrossRef]

21. Allard, R.; Smith, T.A.; Jensen, T.G.; Chu, P.Y.; Roger, E.; Campbell, T.J. *Validation Test Report for the Coupled Ocean/Atmosphere Mesoscale Prediction System (COAMPS) Version 5.0: Ocean/Wave Component Validation*; NRL Technical Memorandum Report; NRL/MR/7320--12-9423; Naval Research Laboratory: Washington, DC, USA; Stennis Space Center: Hancock County, MS, USA, 2012; p. 91.

22. McDonnell, A.M.; Buesseler, K.O. Variability in the average sinking velocity of marine particles. *Limnol. Oceanogr.* **2010**, *55*, 2085–2096. [CrossRef]

23. Maggi, F. The settling velocity of mineral, biomineral, and biological particles and aggregates in water. *J. Geophys. Res. Oceans* **2013**, *118*, 2118–2132. [CrossRef]

24. Portela, L.I.; Ramos, S.; Trigo-Teixeira, A. Effect of salinity on the settling velocity of fine sediments of a harbour basin. *J. Coast. Res.* **2013**, *65*, 1188–1193. [CrossRef]

25. Virmani, J.I.; Weisberg, R.H. Features of the Observed Annual Ocean-Atmosphere Flux Variability on the West Florida Shelf. *J. Clim.* **2003**, *16*, 734–745. [CrossRef]

26. Vidal, V.M.V.; Vidal, F.V.; Hernández, A.F.; Meza, E.; Zambrano, L. Winter water mass distributions in the western Gulf of Mexico affected by a colliding anticyclonic ring. *J. Oceanogr.* **1994**, *50*, 559–588. [CrossRef]

27. Jolliff, J.K.; Kindle, J.C.; Penta, B.; Helber, R.; Lee, Z.; Shulman, I.; Arnone, R.A.; Rowley, C. On the relationship between satellite-estimated bio-optical and thermal properties in the Gulf of Mexico. *J. Geophys. Res. Biogeosci.* **2008**, *113*, G010204. [CrossRef]

28. Portela, E.; Tenreiro, M.; Pallàs-Sanz, E.; Meunier, T.; Ruiz-Angulo, A.; Sosa-Gutiérrez, R.; Cusí, S. Hydrography of the central and western Gulf of Mexico. *J. Geophys. Res. Ocean.* **2018**, *123*, 5134–5149. [CrossRef]

29. Lee, Z.P.; Carder, K.L.; Arnone, R.A. Deriving inherent optical properties from water color: A multiband quasi-analytical algorithm for optically deep waters. *Appl. Opt.* **2002**, *41*, 5755–5772. [CrossRef] [PubMed]

30. Mellor, G.L.; Yamada, T. Development of a turbulence closure model for geophysical fluid problems. *Geophys. Rev.* **1982**, *20*, 851–875. [CrossRef]

31. Ondrusek, M.; Stengel, E.; Kinkade, C.S.; Vogel, R.L.; Keegstra, P.; Hunter, C.; Kim, C. The development of a new optical total suspended matter algorithm for the Chesapeake Bay. *Remote Sens. Environ.* **2012**, *119*, 243–254. [CrossRef]

32. Nechad, B.; Ruddick, K.G.; Park, Y. Calibration and validation of a generic multisensor algorithm for mapping of total suspended matter in turbid waters. *Remote Sens. Environ.* **2010**, *114*, 854–866. [CrossRef]

33. Yeom, J.-M.; Kim, H.-O. Comparison of NDVIs from GOCI and MODIS Data towards Improved Assessment of Crop Temporal Dynamics in the Case of Paddy Rice. *Remote Sens.* **2015**, *7*, 11326–11343. [CrossRef]

34. Ryu, J.-H.; Han, H.-J.; Cho, S.; Park, Y.-J.; Ahn, Y.-H. Overview of geostationary ocean color imager (GOCI) and GOCI data processing system (GDPS). *Ocean Sci. J.* **2012**, *47*, 223–233. [CrossRef]

35. Li, Z.; Roy, D.P.; Zhang, H.K. The incidence and magnitude of the hot-spot bidirectional reflectance distribution function (BRDF) signature in GOES-16 Advanced Baseline Imager (ABI) 10 and 15 minute reflectance over north America. *Remote Sens. Environ.* **2021**, *265*, 112638. [CrossRef]

36. He, R.; Weisberg, R.H. West Florida Shelf circulation and temperature budget for the 1999 spring transtition. *Cont. Shelf Res.* **2002**, *22*, 719–748. [CrossRef]

37. Weisberg, R.H.; Liu, Y. Local And Deep-Ocean Forcing Effects on the West Florida Continental Shelf Circulation and Ecology. *Front. Mar. Sci.* **2022**, *9*, 863227. [CrossRef]

38. Sorinas, L.; Weisberg, R.H.; Liu, Y.; Law, J. Ocean-atmosphere heat exchange seasonal cycle on the West Florida Shelf derived from long term moored data. *Deep Sea Res. Part II Top. Stud. Oceanogr.* **2023**, *212*, 105341. [CrossRef]

39. Fernandez-Partagas, J.; Mooers, C.N.K. A Subsynoptic Study of Winter Cold Fronts in Florida. *Mon. Wea. Rev.* **1975**, *103*, 742–744. [CrossRef]

40. Zavala-Hidalgo, J.; Romero-Centeno, R.; Mateos-Jasso, A.; Morey, S.L.; Martínez-López, B. The response of the Gulf of Mexico to wind and heat flux forcing: What has been learned in recent years? *Atmósfera* **2014**, *27*, 317–334. [CrossRef]

41. Chapman, D.C.; Gawarkiewicz, G. On the establishment of the seasonal pycnocline in the Middle Atlantic Bight. *J. Phys. Oceanogr.* **1993**, *23*, 2487–2492. [CrossRef]

42. Morey, S.L. The spring transition from horizontal to vertical thermal stratification on a midlatitude continental shelf. *J. Geophys. Res.* **2002**, *107*, 0148–0227. [CrossRef]

43. Pasqueron de Fommervault, O.; Perez-Brunius, P.; Damien, P.; Camacho-Ibar, V.F.; Sheinbaum, J. Temporal variability of chlorophyll distribution in the Gulf of Mexico: Bio-optical data from profiling floats. *Biogeosciences* **2017**, *14*, 5647–5662. [CrossRef]

44. Etter, P.C. Heat and Freshwater Budgets of the Gulf of Mexico. *J. Phys. Oceanogr.* **1983**, *13*, 2058–2069. [CrossRef]

45. Kamykowski, D.; Pridgen, K.G.; Morrison, J.M.; McCulloch, A.A.; Nyadjro, E.S.; Thomas, C.A.; Sinclair, G.A. Cold front induced changes on the Florida panhandle shelf during October 2008. *Cont. Shelf Res.* **2013**, *54*, 52–66. [CrossRef]

46. Conmy, R.N.; Coble, P.G.; Cannizzaro, J.P.; Heil, C.A. Influence of extreme storm events on West Florida Shelf CDOM distributions. *J. Geophys. Res. Biogeosciences* **2009**, *114*. [CrossRef]

47. Del Castillo, C.E.; Coble, P.G.; Conmy, R.N.; Müller-Karger, F.E.; Vanderbloemen, L.; Vargo, G.A. Multispectral in situ measurements of organic matter and chlorophyll fluorescence in seawater: Documenting the intrusion of the Mississippi River plume in the West Florida Shelf. *Limnol. Oceanogr.* **2001**, *46*, 1836–1843. [CrossRef]

48. Werdell, P.J.; McKinna, L.I.; Boss, E.; Ackleson, S.G.; Craig, S.E.; Gregg, W.W.; Lee, Z.; Maritorena, S.; Roesler, C.S.; Rousseaux, C.S.; et al. An overview of approaches and challenges for retrieving marine inherent optical properties from ocean color remote sensing. *Prog. Oceanogr.* **2018**, *160*, 186–212. [CrossRef] [PubMed]

49. Lachlan, I.; McKinna, W.; Werdell, P.J. Approach for identifying optically shallow pixels when processing ocean-color imagery. *Opt. Express* **2018**, *26*, A915–A928.

50. Meyer, C.A.; Pu, R. Seagrass resource assessment using remote sensing methods in St. Joseph Sound and Clearwater Harbor, Florida, USA. *Environ. Monit. Assess.* **2012**, *184*, 1131–1143. [CrossRef] [PubMed]

51. Louchard, E.M.; Reid, R.P.; Stephens, C.F.; Davis, C.O.; Leathers, R.A.; Downes, T.V.; Maffione, R. Derivative analysis of absorption features in hyperspectral remote sensing data of carbonate sediments. *Opt. Express* **2002**, *10*, 1573–1584. [CrossRef] [PubMed]

52. Barnes, B.B.; Hu, C.; Schaeffer, B.A.; Lee, Z.; Palandro, D.A.; Lehrter, J.C. MODIS-derived spatiotemporal water clarity patterns in optically shallow Florida Keys waters: A new approach to remove bottom contamination. *Remote Sens. Environ.* **2013**, *134*, 377–391. [CrossRef]

53. Weisberg, R.H.; Zheng, L.; Liu, Y. West Florida shelf upwelling: Origins and pathways. *J. Geophys. Res. Ocean.* **2016**, *121*, 5672–5681. [CrossRef]

54. Liu, Y.; Weisberg, R.H. Seasonal variability on the West Florida shelf. *Prog. Oceanogr.* **2012**, *104*, 80–98. [CrossRef]

55. Huguenard, K.D.; Bogucki, D.J.; Ortiz-Suslow, D.G.; MacMahan, J.H. Nearshore response to cold air outbreaks in the Gulf of Mexico. *Estuar. Coast. Shelf Sci.* **2020**, *235*, 106604. [CrossRef]

56. Noh, Y.; Ok, H.; Lee, E.; Toyoda, T.; Hirose, N. Parameterization of Langmuir Circulation in the Ocean Mixed Layer Model Using LES and Its Application to the OGCM. *J. Phys. Oceanogr.* **2016**, *46*, 57–78. [CrossRef]

57. Shrestha, K.; Anderson, W.; Kuehl, J. Langmuir turbulence in coastal zones: Structure and length scales. *J. Phys. Oceanogr.* **2018**, *48*, 1089–1115. [CrossRef]

58. Green, M.O.; Coco, G. Review of wave-driven sediment resuspension and transport in estuaries. *Rev. Geophys.* **2014**, *52*, 77–117. [CrossRef]

59. Wiberg, P.L.; Sherwood, C.R. Calculating wave-generated bottom orbital velocities from surface-wave parameters. *Comput. Geosci.* **2008**, *34*, 1243–1262. [CrossRef]